# Validation of massively parallel free-surface SPH simulations of gravity-driven flow and partitioning dynamics at complex fracture intersections

Jannes Kordilla
Torsten Noffz
Department of Applied Geosciences
University of Goettingen
Goettingen, Germany
jkordil@gwdg.de

Alexandre Tartakovsky
Computational Mathematics Group
Pacific Northwest National Laboratory
Richland, USA
Alexandre.Tartakovsky@pnnl.gov

***Abstract*—Flow velocities of water in porous geological media generally do not exceed a few millimeters per day. However, tectonic stresses commonly induce the formation of discontinuities, i.e. fractures, which allow much higher flow velocities. In the case of vertical, gravity-driven flows, this leads to a pronounced deviation from classical volume-effective descriptions and complicates the prediction of water movement for example in the context of nuclear waste repository sites, mining industry and in general water resources management. On fracture-scales the spatial and temporal distribution of flow modes and its influence on travel time distributions is still not very well understood. The complex interplay of flow modes such as droplets, rivulets, turbulent and adsorbed films and its relation to the geometrical properties of the system is difficult to model and requires efficient numerical methods. We conducted laboratory-scale percolation experiments of multiphase (free-surface) flow through synthetic fracture systems. The setup allows us to obtain travel time distributions and identify characteristic flow mode distributions on wide aperture fractures intercepted by horizontal fracture elements. The effect of flow mode formation on fracture partitioning dynamics is demonstrated.**

## I. Introduction

Fractured porous media are one of the the most challenging system to study in terms of saturated and specifically unsaturated (that is, multiphase flow in the presence of an airphase) flow and transport dynamics. The highly non-linear behavior of dependent variables in space and time and various interactions of scale-dependent components clearly qualify such media as complex systems [1]. Understanding and predicting unsaturated flow dynamics in fractured media is of high importance for various applications. Up to 75% of the worldwide aquifers [2] consist of fractured and karstified aquifers and therefore are an important target for water resources management and vulnerability assessment [3]. Geotechnical applications such as tunneling, mining, construction of damns and landfills heavily depend on a thorough characterization of flow and pressure fields to warrant long-term stability of the respective structures [4], [5]. Furthermore, the safety of potential subsurface nuclear waste disposal sites heavily depends on a clear understanding of flow and transport through the overlying unsaturated (vadose) zone and potential leakage caused by connectivity to fracture networks e.g. [3], [6].

However, on fracture and fracture-network scales unsaturated flow and transport through geological media are still poorly understood, mainly due to the missing insight into the detailed flow processes. Small-scale laboratory experiments for gravity-driven unsaturated flow are rarely carried out and often exhibit erratic or chaotic flow dynamics e.g. [7]–[10]. Flow modes in general evolve with increasing flow rates from thin adsorbed films over droplets and rivulets to wavy surface films [11], [12] and may coexist. Consequently results are difficult to cast into a meaningful framework without the help of additional numerical modeling. This especially concerns the complex flow dynamics at fracture intersections, which act as a neuralgic point as they (1) control the overall connectivity of fracture networks [13] (2) the partitioning behavior in between connected fracture elements [10] and ultimately (3) the distribution of flow modes on fracture surfaces, which in turn affect the interaction between porous matrix and fracture e.g. [14], [15].

Numerical models for this class of fluid flow problems have to resolve various demanding properties, such as the complex evolution of fluid-air interfaces, formation of singularities (e.g. droplet breakups), flow mode switching, dynamic contact angles and complex solid geometries of rough fracture surfaces. Lagrangian methods such as SPH, dissipative particle dynamics (DPD) or molecular dynamics (MD) provide a meshfree interpolation of the governing partial differential equations. Among these three methods SPH can be considered a macroscopic method as it commonly relies on Navier-Stokes continuum description of the flow field. Due to the properties of the Lagrangian framework, SPH provides several advantages, specifically in the case of free-surface flow dynamics: (1) Momentum, mass and energy are explicitly conserved, (2) multiphase interfaces are explicitly represented by individual particles and do not require front-tracking algorithms, (3) free surfaces (fluid-gas interfaces) can be easily modeled, thus saving computational resources, (4)

physical phenomena such as surface tension naturally arise from pairwise particle interactions and (5) viscosity can be efficiently prescribed without non-linear advection terms in the momentum conservation equation.

In this work we employ a highly parallelized SPH code that we implemented within the LAMMPS (Large-scale atomic/molecular massively parallel simulator, [16], [17]) framework. In its original form LAMMPS has been developed for MD simulations, however, due to the similarities between SPH and MD in terms of the numerical algorithms (e.g. particle-based flow field, link-lists, nearest neighbor search), many features are also beneficial for SPH applications. This includes a domain-based decomposition of the particle field for an efficient MPI parallelization and an adaptive processor allocation, i.e. dynamic load balancing. Specifically the latter feature becomes important when simulations consist of sparsely populated domain (e.g. in the case of free-surface flows), in order to optimize the per-processor particle load.

Our SPH code was validated for various applications, such as free-surface flow in smooth and rough fractures [18], [19], flow and transport dynamics in porous media [20], [21], mesoscale modeling of advection-diffusion phenomena [22], reaction and mixing kinetics in porous media [21], [23], [24] and modeling of surface tension and contact angles [18], [25]–[27].

The main objective of this work is to identify important parameters that affect flow partitioning dynamics of gravity-driven free-surface flows at horizontal fracture intersection. The effect of flow mode formation on the travel time distribution is demonstrated via highly parallelized three-dimensional SPH simulations and laboratory experiments which serve as a validation for our new SPH code. The efficiency of horizontal fracture imbibition is shown to depend on the type of flow mode that prevails on the vertical fracture surface and flowrate dependent scaling behavior is observed.

## II. Methods

### A. Smoothed Particle Hydrodynamics

Here we give a brief description of our SPH model.

Noting that $r = |\mathbf{r} - \mathbf{r}'|$ we employ the following kernel in terms of relative distances $q = r/h$ as [28] which was shown to have superior stability properties [29]

$$W(q,h) = \alpha_k \begin{cases} (1-q)^3 & 0 \le q < 1 \\ 0 & 1 \le q\,. \end{cases} \tag{1}$$

where $\alpha_k = 168/(16\pi h^3)$.

The following discretization of the NS equation conserves momentum exactly due to the symmetric pressure gradient [30] and employs a common discretization of the viscous diffusion terms [31]:

$$\begin{aligned} \frac{d\mathbf{v}_i}{dt} =& \sum_{j=1}^{N} m_j \left( \frac{P_i}{\rho_i^2} + \frac{P_j}{\rho_j^2} \right) \hat{\mathbf{e}}_{ij} \frac{\partial W(\mathbf{r}_{ij}, h)}{\partial r_{ij}} \\ &+ \sum_{j=1}^{N} m_j \frac{\mu_i + \mu_j}{\rho_i \rho_j} \frac{\mathbf{v}_{ij}}{r_{ij}} \frac{\partial W(\mathbf{r}_{ij}, h)}{\partial r_{ij}} \\ &+ \sum_{j=1}^{N} \frac{1}{m_j} \mathbf{f}_{ij} + \mathbf{g}\,, \end{aligned} \tag{2}$$

where $\hat{\mathbf{e}}_{ij} = \mathbf{r}_{ij}/r_{ij}$ is the unit vector pointing from particle $i$ to particle $j$ and $\mathbf{f}_{ij}$ is a conservative interaction force that creates surface tension [25]. The force is constructed from two superposed cubic spline functions of the form [18]

$$W(q,h) = \alpha_k \begin{cases} 1 - \frac{3}{2}(q)^2 + \frac{3}{4}(q)^3 & 0 \le q < 1 \\ \frac{1}{4}(2-q)^3 & 1 \le q < 2 \\ 0 & 2 \le q\,. \end{cases} \tag{3}$$

where $q = 2r/h$ such that $\mathbf{f}_{ij}$

$$\mathbf{f}_{ij} = s_{ff}(AW_1(r_{ij}, h_1) - BW_2(r_{ij}, h_2))\hat{\mathbf{e}}_{ij}\,. \tag{4}$$

Here $A = (h_1/h_2)^3$, $B = 1$, $h_1 = h$ and $h_2/h_1 = 2$.

In order to close the equation system Eq. (2) the density $\rho$ and pressure $P$ of each particle have to be computed during each time step. The density is evaluated via kernel summation as

$$\rho_i = \sum_{j=1}^{N} m_j W(\mathbf{r}_{ij}, h)\,. \tag{5}$$

The pressure is obtained from an equation of state (EOS) following [32], [33]

$$P(\rho) = B\left( \left[ \frac{\rho}{\rho_0} \right]^{\gamma} - 1 \right) + P_0\,, \tag{6}$$

where $\rho_0$ is the reference density and $P_0$ is a background pressure. The scaling constant $B$ is given by

$$B = c^2 \frac{\rho_0}{\gamma}\,, \tag{7}$$

with $c$ being the speed of sound and $\gamma$ is a coefficient commonly set to $\gamma = 7$ to achieve a rapid pressure increase for approaching particles and avoid penetration of solid boundaries. The speed of sound is problem dependent and is chosen such that the fluid behaves nearly incompressible, that is, $|\delta\rho|/\rho \le 0.03$ which was shown to be sufficient to model accurate pressure fields [31]. Fluid particles that approach a boundary are subject to a high acceleration due to the attractive component of the interaction force Eq. (4), such that the effect of the pressure gradient alone may not be sufficient to avoid penetration. A common method to address this problem and prescribe no-slip boundary conditions was developed by [34] who employed ghost particles that mirror fluid particles normal to the nominal solid interface with inversed velocity. This methods was enhanced for example by [31], [35]. However,

the determination of the nominal solid boundary becomes challenging for highly irregular surfaces and the computational costs are high compared to simpler bounce-back conditions, as demonstrated e.g. by [18], [26], [36]. In this work we opt for the later solution combined with the proximity ratio determination of [37]. To approximate the nominal solid-fluid boundary within the diffuse interface region of an irregular surface a state-specific number density is employed

$$n^s_{i,\alpha} = \sum \delta_{\alpha,\beta} W(\mathbf{r}_{i,\alpha} - \mathbf{r}_{j,\beta}, h) \tag{8}$$

where the Kronecker delta is defined as

$$\delta_{\alpha,\beta} = \begin{cases} 1 & \alpha = \beta \\ 0 & \alpha \neq \beta \end{cases} \tag{9}$$

and $\alpha$ and $\beta$ denote the state of a particle (in the sense of a color function) that can either belong to the fluid or the solid region. Now a proximity ratio can be defined as

$$\phi_i = \frac{n^s_i}{n_i}\,, \tag{10}$$

where $n_i$ is the actual number density of a particle. For a straight interface in between two phases, e.g. solid-fluid or fluid-fluid, this ratio evaluates to

$$\phi_i = \begin{cases} 0.5 & x_i \\ \epsilon\,]0.5, 1[ & 0 < x_i < h \\ 1 & x_i \geq h \end{cases}\,, \tag{11}$$

where $x_i$ is the distance to the nominal interface, which is located at a distance equal to half of the inter-particle spacing $\Delta x = (m/\rho)^{1/3}$ normal to the interface. In order to enforce a no-slip boundary condition we return fluid particles along the normal of the fluid interface to the flow field once they penetrate the boundary, i.e. when $\phi_i < 0.5$. The normals are calculated using a color function:

$$c_i = \sum_{j=1}^{N} \frac{m_j}{\rho_j} \psi_j W(\mathbf{r}_{ij}, h)\,, \tag{12}$$

where $\psi_j = 1$ for fluid particles and zero for solid particles, such that the normals can be obtained from the gradient

$$\mathbf{n}_i = \nabla c_i\,. \tag{13}$$

Particles that penetrate the boundary are returned along the fluid normal by a distance $\Delta d$ proportional to the proximity ratio:

$$\Delta d = \beta \Delta x (1 - \frac{\phi_i}{0.5})\,, \tag{14}$$

where we found $\beta = 2$ to give best results for various values of surface tension and wall geometries. It should be noted that the bounce-back condition is commonly only activated when fluid particles initially come into contact with a solid boundary, i.e. fluid-solid interaction forces create a strong acceleration.

Equation (2) is integrated using a modified Velocity-Verlet time stepping scheme. Noting that

$$\frac{d\mathbf{r}_i}{dt} = \mathbf{v}_i \qquad \text{and} \qquad \mathbf{a}_i = \frac{\mathbf{f}_i}{m_i}\,, \tag{15}$$

where $\mathbf{a}_i$ is the acceleration, the time stepping scheme is given as

$$\mathbf{v}_i(t + \tfrac{1}{2}\Delta t) = \mathbf{v}_i + \tfrac{1}{2}\mathbf{a}_i(t) \tag{16a}$$

$$\bar{\mathbf{v}}_i(t + \Delta t) = \mathbf{v}_i(t) + \Delta t \mathbf{a}_i \tag{16b}$$

$$\mathbf{r}_i(t + \Delta t) = \mathbf{r}_i(t) + \Delta t \mathbf{v}_i(t + \tfrac{1}{2}\Delta t) \tag{16c}$$

Calculation of $\mathbf{a}_i(t + \Delta t)$ using extrapolated velocity $\bar{\mathbf{v}}_i$

$$\mathbf{v}_i(t + \Delta t) = \mathbf{v}_i(t + \tfrac{1}{2}\Delta t) + \frac{1}{2}\mathbf{a}_i(t + \Delta t) \tag{16d}$$

Particle mass can be obtained as $m = \rho_0 \Delta x^3$, where $\Delta x$ is the inter particle spacing. The kernel length is obtained from $h = n^{1/3}\Delta x$, where $n = 40$. Solid walls consists of three layers of particles in order to satisfy the normalization condition for fluid particle in the vicinity of the solid walls.

### B. Laboratory setup

For the percolation experiment we use an 24 channel laboratory dispenser (Ismatec® IPC High Precision Multichannel Dispenser ISM934C) and silicon tubes with an inner diameter of $1.5\,\mathrm{mm}$. The cubes have dimensions of $20 \times 20 \times 20\,\mathrm{cm}$ and are made of clear polymethylmethacrylat (PMMA). Static contact angles $\theta_0$ of the surfaces are $65.16°(\pm 2.91°)$ and were experimentally determined with a contact angle goniometer. Sessile droplets had an average volume of $1.74\,\mu\mathrm{L}$ ($\pm 0.12\,\mu\mathrm{L}$).

The experimental setup is shown in Fig. 1. Cubes are stacked on top of each other separated by four metallic distance spacers with varying thickness $d_f$ and a diameter of $5\,\mathrm{mm}$. The base of the experimental setup consists of a metallic square grill with cell sizes of $5 \times 5 \times 5\,\mathrm{cm}$ and was coated with a hydrophobic lacquer ($\theta_0 \approx 110°$) to maximize flow velocities across the grill. The drip water is collected by a digital scale beneath the grill at an accuracy of $0.1\,\mathrm{ml}$. The additional travel time from the bottom of the cubes into the drip collector was experimentally determined to lie below $500\,\mathrm{ms}$ and does not influence the overall results significantly. Evaporation rates from the collector pan were determined for a constant room temperature and are accounted for during the experiments. We use distilled water for all experiments, however, fluorescent dye (uranine) was added to increase visibility in some of the figures.

## III. Results

### A. General validation experiments

While the model has been validated for various types of flow dynamics (e.g. [18], [19], [27] here we show a simple numerical experiment to determine maximum droplet heights. Sessile droplets assume a spherical cap shape when their radius $r$ is small compared to the capillary length

$$\lambda_c = \sqrt{\frac{\gamma}{\rho g}}\,, \tag{17}$$

i.e. $r \ll \lambda_c$, whereas larger droplets tend to be flattened by gravitational effects which limit the maximum height $h_{max}$.

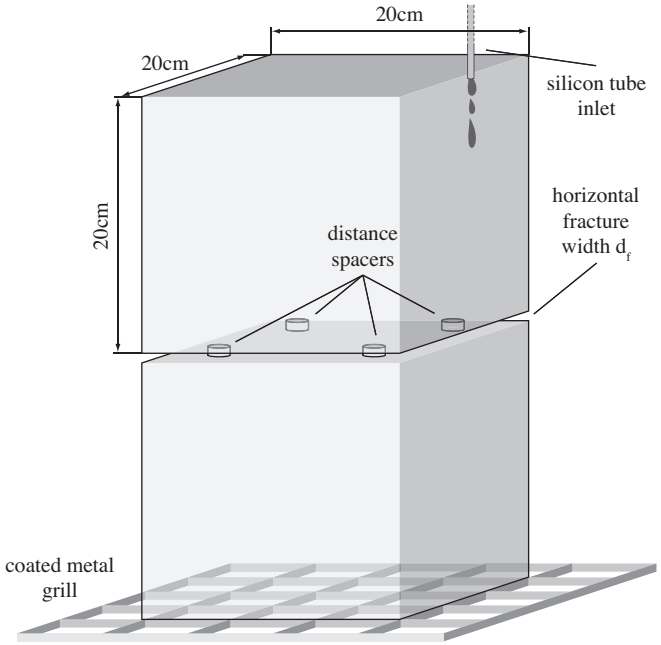


Fig. 1. Sketch of the laboratory setup.

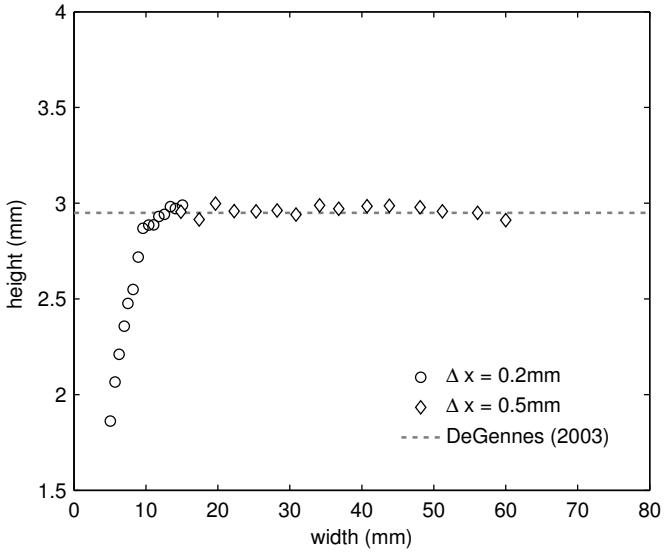


Fig. 2. Droplet heights for two resolutions and several droplet radii. Droplet with a radius much larger than the capillary length are flattened by the effect of gravity and establish a maximum height, i.e. form fluid puddles.

The maximum height can be approximated by [38]:

$$h_{max} = 2\lambda_c sin\left(\frac{\theta_0}{2}\right), \tag{18}$$

where $\theta_0$ is the static contact angle between fluid and solid surface. Figure 2 shows the maximum droplet height obtained for two different resolutions of our SPH model and several droplet radii. At both resolutions we obtain a good convergence to the theoretical solution. Some fluctuation around the theoretical value can be attributed to the partially not perfectly flat top surface of the droplets, as we do not determine an averaged maximum height along the top surface.

### *B. Low resolution simulations*

Our initial laboratory setup consisted of 15 injection points (here referred to as point-wise or localized injection) equally distributed along the top of the upper cube where each outlet has a flow rate of $2.5\,\mathrm{mL\,min^{-1}}$. The cubes are separated by a distance of $2.5\,\mathrm{mm}$. During the experiments the accumulated fluid mass that reached the bottom of the system was measured using the digital scale. A second inlet condition (diffuse boundary) was created by placing a thin sponge along the whole length of the cube in front of the tube outlets. This setup was intended to mimic a diffuse type of boundary condition, e.g. by an overlying fine-grained soil layer. Laboratory experiments display a rather high variation in terms of the first arrival times at the bottom of the system and the time-dependent partitioning dynamics at the fracture intersection. Therefore we conducted several experiments for each boundary condition in order to detect a characteristic behavior. The numerical simulations were setup with the following parameters: $\rho_{f,0} = 930\,\mathrm{kg\,m^{-3}}$, $\rho_{s,0} = 1000\,\mathrm{kg\,m^{-3}}$, $c_0 = 1.5\,\mathrm{m\,s^{-1}}$, $s_{ff} = 3.0 \times 10^{-5}\,\mathrm{kg\,m\,s^{-2}}$, $s_{sf} = 8.0 \times 10^{-6}\,\mathrm{kg\,m\,s^{-2}}$ and consisted of approximately 3 million particles with an inter particle spacing of $\Delta x = 5.0 \times 10^{-4}\,\mathrm{m}$ (see Fig. 3). With the given interaction parameters the surface tension is $\sigma \approx 0.07$ [18] and the static contact angle is $\theta_0 \approx 65°$. Due to the long simulation times only a limited set of simulations was performed and compared to the laboratory experiments for early times of the experiments $t$ <50 s. Figure 4 shows the results of the laboratory experiments and the corresponding SPH simulations. The laboratory experiments indicate a much faster initial arrival time for the point-wise injection followed by a filling of the horizontal fracture and finally a steady-state phase once the fracture is completely filled. The diffuse boundary in general promotes a faster filling of the horizontal fracture and on average later initial arrival times, which also leads to a faster establishment of a steady-state (i.e. inflow = outflow). While we could not conduct the same amount of simulations for this experiment the simulations display a similar behavior for both of the boundary conditions. Simulations and laboratory experiments both favour the formation of a reduced number of rivulets for the diffuse boundary, while the point-wise injection promotes the formation of 15 individual droplet trails. This difference in preferential flow mode is believed to be the major controlling factor of the partitioning dynamic at the fracture intersection. However, a qualitative comparison between the laboratory experiments and SPH simulations revealed a higher number of partial rivulets (i.e. merged droplets) in the numerical experiments for the point-wise injection which is believed to be a result of insufficient resolution, i.e. flow features such as thin rivulets or droplet breakup singularities are not correctly sustained. In the next section we carry out a convergence study to determine

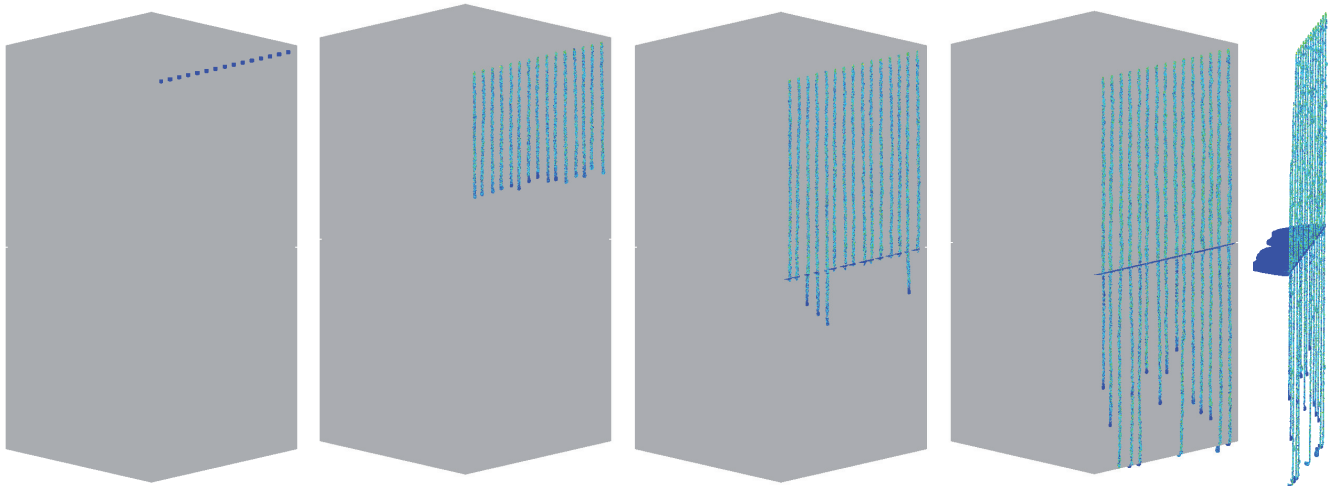

Fig. 3. Example of a point-wise injection simulation at a resolution of $\Delta x = 5.0 \times 10^{-4}\,\mathrm{m}$ and about 3 million particles.

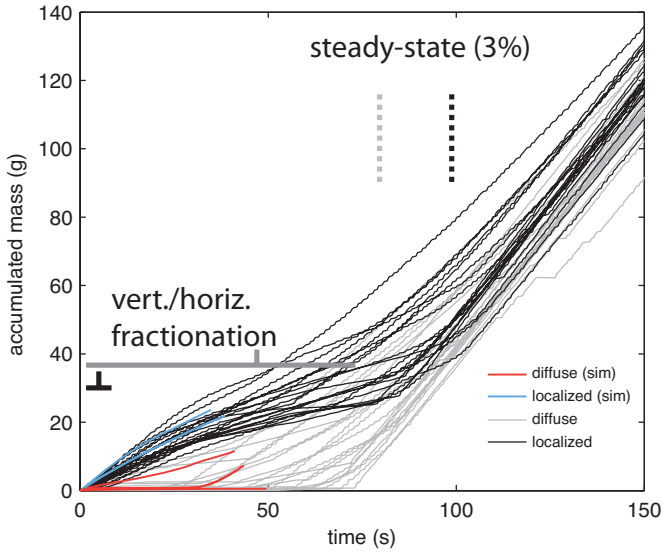


Fig. 4. Comparison of mass accumulation at the system outlet for both boundary conditions and SPH simulations. Point-wise injection boundaries exhibit a much lower variation in initial arrival times, while the diffuse boundary promotes a stronger flow into the horizontal fracture and consequently a later average arrival time. Steady-state is established faster for the diffuse boundary.

an adequate resolution.

### C. High resolution simulations: Flow regime transitions

In order to validate the SPH model for a complex flow setting we conducted a series of laboratory experiments to determine prevailing flow modes for various flow-rates ranging from $1.5\,\mathrm{mL\,min^{-1}}$ to $4.5\,\mathrm{mL\,min^{-1}}$ at different resolutions on a smooth vertical surface. For the given fluid-solid combination the whole spectrum of flow modes (droplets, mixed droplets/rivulet, rivulets) can be observed. Due to environmental "noise" such as slight impurities on the PMMA surfaces and/or tiny air-pressure or flow rate variations [7], [10] it is nearly impossible to establish a perfect droplet regime, i.e. a stream of individual droplets moving at the exact same velocity down the surface. Such interferences commonly induce mixed flow regimes, e.g. merging droplet, that temporarily form partial rivulets or larger droplets that travel at high velocities and emit smaller droplets. While the transition to full rivulet flow can be rather easily determined (a continuous stream is established) the intermediate regimes are rather difficult to compare quantitatively under such conditions. Figure 5 shows a qualitative comparison of our SPH model for three different flow rates. Parameters for the SPH model are $\rho_{f,0} = 950\,\mathrm{kg\,m^{-3}}$, $\rho_{s,0} = 1000\,\mathrm{kg\,m^{-3}}$, $c_0 = 4\,\mathrm{m\,s^{-1}}$, $s_{ff} = 6.5 \times 10^{-6}\,\mathrm{kg\,m\,s^{-2}}$, $s_{sf} = 2.0 \times 10^{-6}\,\mathrm{kg\,m\,s^{-2}}$. The background pressure $P_0$ is set to zero and $\gamma = 7$. The inter-particle spacing is $\Delta x = 1.0 \times 10^{-4}\,\mathrm{m}$ and surface tension $\sigma = 0.07$. The final transition from droplet flow mode to constant rivulet flow mode was found to be at about $3.0\,\mathrm{mL\,min^{-1}}$ ($\pm 0.25\,\mathrm{mL\,min^{-1}}$) and $2.9\,\mathrm{mL\,min^{-1}}$ for the SPH simulations. Three different resolutions ($\Delta x = 0.0001\,\mathrm{m}$, $0.0002\,\mathrm{m}$ and $0.0005\,\mathrm{m}$) were tested and convergence was found approximately at a resolution of $\Delta x = 1.0 \times 10^{-4}\,\mathrm{m}$.

### D. Single inlet fractionation dynamics at horizontal fracture intersections

Similar to the coarse resolution simulations we conducted further numerical and laboratory experiments to investigate the process of fractionation for a single tube inlet and cubes separated by distance spacer with a thickness of $d_f = 2.5\,\mathrm{mm}$. At this spacing the fractionation process at the intersection between horizontal and vertical "fracture" is likely to be controlled by a complex interplay of inertia and capillary forces, i.e. the prevailing flow mode. Distilled water is injected at the top of the upper cube as shown in Fig. 1, such that an immediate capillary connection is established. Flow rates were varied in the range of $1.5\,\mathrm{mL\,min^{-1}}$ to $4.5\,\mathrm{mL\,min^{-1}}$ at an interval of $0.5\,\mathrm{mL\,min^{-1}}$. Each experiment was run for $1.5\,\mathrm{min}$ and the ratio of injected to total water mass was recorded. We carried out 10 experiments at each flow rate. While results

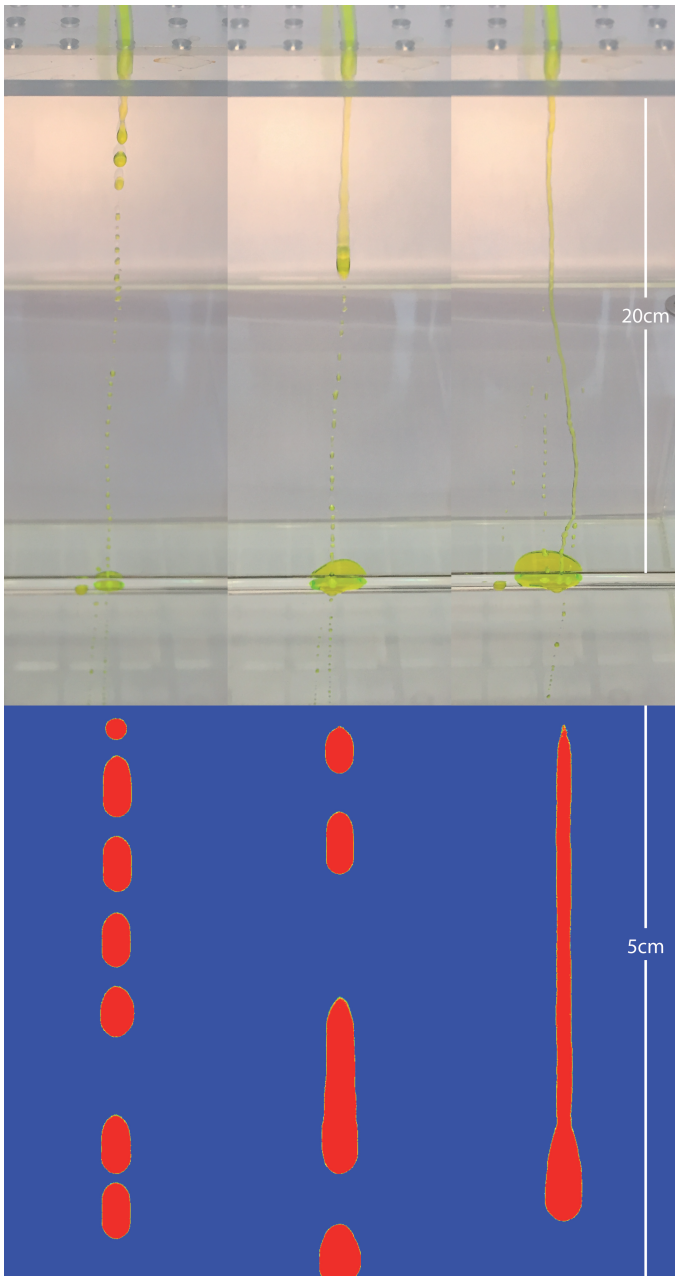


Fig. 5. Flow mode transitions observed in the laboratory and corresponding SPH simulations. (Left) Droplet mode at $1.5\,\mathrm{mL\,min^{-1}}$, (middle) transition zone from droplet to full rivulet flow mode at $2.5\,\mathrm{mL\,min^{-1}}$ and (right) constant rivulet mode at $3.0\,\mathrm{mL\,min^{-1}}$. Note the difference in scale between simulations and experiments.

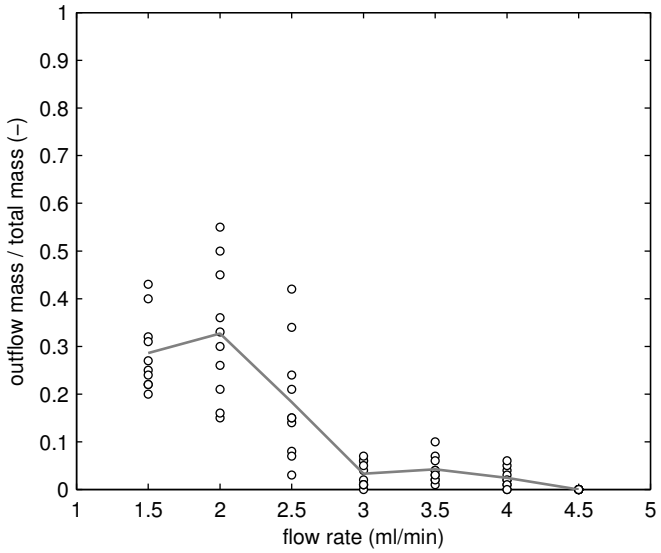


Fig. 6. Ratio of accumulated mass on the scale vs. injected fluid mass. Partitioning behavior at the fracture intersection can be clearly linked to the occurrence of flow modes on the vertical surfaces. For rivulet flows ($>3.0\,\mathrm{mL\,min^{-1}}$) nearly all injected water is stored in the horizontal fracture.

display a certain variation we can identify characteristic trends in the dataset, similar to the initial experiments conducted with 15 inlets. Figure 6 shows the ratio of fluid mass that left the system vs. total injected mass after $90\,\mathrm{s}$. It becomes apparent that at flow rates of $3.0\,\mathrm{mL\,min^{-1}}$ or higher nearly no fluid bypasses the horizontal fracture (until it is fully wetted). At lower flow rates the likelihood increases, whereas in the transition zone between (theoretically) full droplet and rivulet mode experiments exhibit a rather high variance, however, with an increasing average value for decreasing flow rates. Similar Fig. 7 shows the mass accumulation at three different flow rates and the dominating flow modes. While for higher flow rates (i.e. in the rivulet regime) the first breakthrough seems to occur slightly earlier (indicating some bypass) for lower flow rates a much stronger bypass behavior can be observed during the whole experiment. SPH simulations were carried out for several subsets of the laboratory setup in terms of vertical length of the cubes ($5\,\mathrm{cm}$, $10\,\mathrm{cm}$ and $20\,\mathrm{cm}$) at a resolution of $\Delta x = 1.0 \times 10^{-4}\,\mathrm{m}$ which was was shown to be low enough to reproduce important flow features and the transition to full rivulet flow modes. All other parameters are the same as given in III-C. The flow rate was set to $2.0\,\mathrm{mL\,min^{-1}}$ as this should results in (1) fluid bypassing the fracture as well as (2) fluid moving past the fracture intersection. During the laboratory experiments the first breakthrough for a flow rate of $2.0\,\mathrm{mL\,min^{-1}}$ occurred on average after $8.0\,\mathrm{s}$. The simulations for a vertical domain length of $5\,\mathrm{cm}$ and $10\,\mathrm{cm}$ do not result in any fluid bypassing the horizontal fracture during the simulated time span (see see Figure 8. However, the simulations using $20\,\mathrm{cm}$ cubes display the formation of large droplets (initial merging of smaller droplets) which in turn emit smaller droplets that are stuck

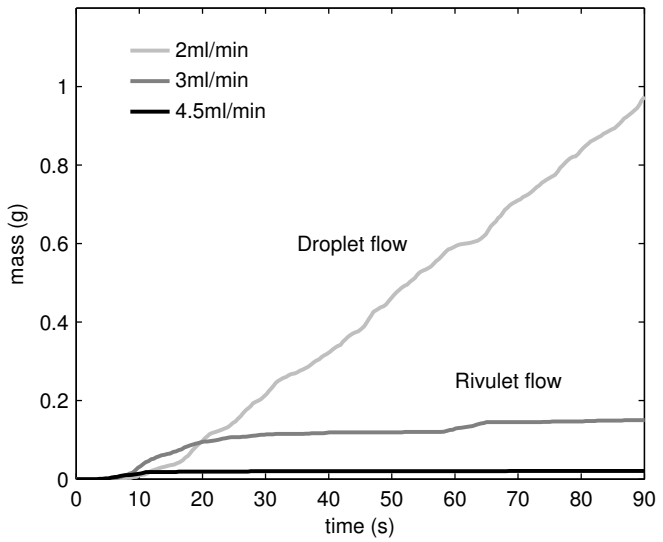


Fig. 7. Outflow mass vs. time for flow rates of $1.5\,\mathrm{mL\,min^{-1}}$, $3.0\,\mathrm{mL\,min^{-1}}$ and $4.5\,\mathrm{mL\,min^{-1}}$) and dominant flow regimes. Data shows an average of 10 experiments for each flow rate.

to the surface. These sessile droplets consequently contribute to the formation of further large droplets which are believed to be able to (partially) bypass the fracture intersection at later times when Bond and Capillary numbers exceed a critical value. At this point our simulations run on 256 cores (about $5\,\mathrm{s}$ simulation time for cubes of $20\,\mathrm{cm}$ length) but could not be carried out long enough to capture the bypass behavior. Figure 8 (right) shows the formation of an early-time merged droplet that was about to bypass the fracture but ultimately gets dragged back by capillary action.

## IV. Conclusion

We employed a parallelized three-dimensional SPH model to study free-surface flow dynamics of complex flows along a simple fracture network intersection. While the studied system at first sight appears to be simple and predictable our laboratory experiments and numerical simulations so far could only narrow down the potential controlling parameters. Further numerical (and laboratory) experiments are necessary to study the partitioning dynamics at the fracture intersection in more detail to obtain a generalized theory. Specifically the vertical domain length seems to heavily influence the dynamics of droplet merging and consequently the increase of both high Bond and Capillary number flow features that are able to bypass the capillary drag of the horizontal fracture. The wetting state of the horizontal fracture is suspected to influence the bypass behavior as well due to the potential decrease in capillary drag with increasing water content.

## Acknowledgment

J. Kordilla was partially supported by DFG SA 501/26-1.

## References

[1] B. Faybishenko, S. M. Benson, and J. E. Gale, *Dynamics of Fluids and Transport in Complex Fractured-Porous Systems*. Washington D.C.: John Wiley & Sons, Ltd., 2015.

[2] P. Dietrich, R. Helmig, M. Sauter, H. Hötzl, J. Köngeter, and G. Teutsch, *Flow and Transport in Fractured Porous Media*. Berlin/Heidelberg: Springer-Verlag, 2005.

[3] A. L. Flint, L. E. Flint, G. S. Bodvarsson, E. M. Kwicklis, and J. Fabryka-Martin, "Evolution of the conceptual model of unsaturated zone hydrology at Yucca Mountain, Nevada," *Journal of Hydrology*, vol. 247, no. 1-2, pp. 1–30, Jun. 2001.

[4] Y. B. Koffi, K. E. Ahoussi, K. E. Kouadio, a. M. Kouassi, O. Kouassi, L. C. Kpangui, and J. Biemi, "Study of the vulnerability of fractured aquifers in the context of an implementation of a modern landfill: application of remote sensing and the geotechnical method on the site of Kossihouen (Cote d' Ivoire, West Africa)," *International Journal of Innovation and Applied Studies*, vol. 2, no. 4, pp. 556–573, 2013.

[5] D. D. Evans and T. C. Rasmussen, "Unsaturated Flow and Transport Through Fractured Rock Related to High-level Waste Repositories: Final Report–phase III," Office of Nuclear Regulatory Research, Washington, Tech. Rep., 1991.

[6] B. a. Ebel and J. R. Nimmo, "An Alternative Process Model of Preferential Contaminant Travel Times in the Unsaturated Zone: Application to Rainier Mesa and Shoshone Mountain, Nevada," *Environmental Modeling & Assessment*, Nov. 2012.

[7] T. R. Wood and H. Huang, "Experimental and modeling studies of episodic air-water two-phase flow in fractures and fracture networks," in *Fluid Dynamics in Complex Fractured-Porous Systems*. John Wiley & Sons, Ltd., 2015, p. 209.

[8] M. J. Nicholl and R. J. Glass, "Infiltration into an Analog Fracture," *Vadose Zone Journal*, vol. 4, no. 4, p. 1123, 2005.

[9] G. W. Su, J. T. Geller, K. Pruess, and J. R. Hunt, "Solute transport along preferential flow paths in unsaturated fractures," *Water Resources Research*, vol. 37, no. 10, pp. 2481–2491, 2001.

[10] M. I. Dragila and N. Weisbrod, "Fluid motion through an unsaturated fracture junction," *Water Resources Research*, vol. 40, pp. 1–11, 2004.

[11] T. A. Ghezzehei, "Constraints for flow regimes on smooth fracture surfaces," *Water Resources Research*, vol. 40, pp. 1–14, 2004.

[12] M. I. Dragila and S. Wheatcraft, "Free-surface films," in *Conceptual Models of Flow and Transport in the Fractured Vadose Zone*. National Academies Press, 2001, pp. 217–241.

[13] P. Adler, J.-F. Thovert, and V. Mourzenko, *Fractured Porous Media*. Oxford University Press, 2012.

[14] T. K. Tokunaga and J. Wan, "Water film flow along fracture surfaces of porous rock," *Water Resources Research*, vol. 33, no. 6, p. 1287, 1997.

[15] T. K. Tokunaga, "Hydraulic properties of adsorbed water films in unsaturated porous media," *eScholarship University of California*, 2009.

[16] S. Plimpton, "Fast parallel algorithms for short-range molecular dynamics," *Journal of Computational Physics*, vol. 117, no. 1, pp. 1–19, 1995.

[17] S. Plimpton, P. Crozier, and A. Thompson, "LAMMPS-large-scale atomic/molecular massively parallel simulator," *Sandia National Laboratories*, vol. 18, 2007.

[18] J. Kordilla, A. Tartakovsky, and T. Geyer, "A Smoothed Particle Hydrodynamics model for droplet and film flow on smooth and rough fracture surfaces," *Advances in Water Resources*, vol. 59, pp. 1–14, May 2013.

[19] A. Tartakovsky and P. Meakin, "Simulation of Unsaturated Flow in Complex Fractures Using Smoothed Particle Hydrodynamics," *Vadose Zone Journal*, vol. 4, no. 3, pp. 848–855, 2005.

[20] M. Gouet-Kaplan, A. Tartakovsky, and B. Berkowitz, "Simulation of the interplay between resident and infiltrating water in partially saturated porous media," *Water Resources Research*, vol. 45, no. 5, pp. 1–9, May 2009.

[21] A. Tartakovsky, A. L. Ward, and P. Meakin, "Pore-scale simulations of drainage of heterogeneous and anisotropic porous media," *Physics of Fluids*, vol. 19, no. 10, p. 103301, 2007.

[22] J. Kordilla, W. Pan, and A. Tartakovsky, "Smoothed particle hydrodynamics model for Landau-Lifshitz-Navier-Stokes and advection-diffusion equations," *The Journal of Chemical Physics*, vol. 141, p. 224112, 2014.

[23] A. Tartakovsky, D. Tartakovsky, T. D. Scheibe, and P. Meakin, "Hybrid simulations of reaction-diffusion systems in porous media," *SIAM J. Sci. Comput.*, vol. 30, no. 6, pp. 2799–2816, 2008.

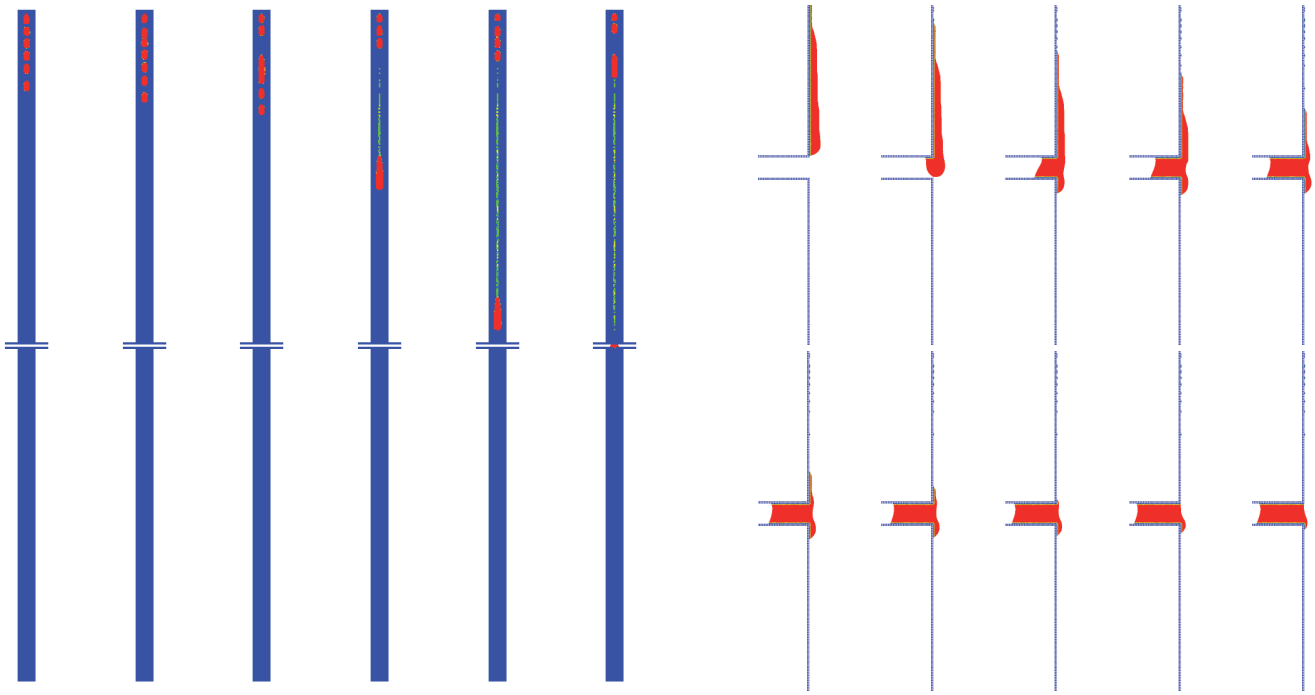

Fig. 8. Simulation of flow on two surfaces of 20 cm height separated by a horizontal fracture at a flow rate of $2.0\,\mathrm{mL\,min^{-1}}$. Total particle number is 4.4 million. (Left) Evolution from a continuous train of droplets to a single rapid merged droplet. (Right) Detailed view of the flow behavior at the intersection shown at $t$ =2.56 s to 2.94 s. A bypass is initiated but reversed due to the capillary drag of the fracture.


[24] A. Tartakovsky, G. Redden, P. C. Lichtner, T. D. Scheibe, and P. Meakin, "Mixing-induced precipitation: Experimental study and multiscale numerical analysis," *Water Resources Research*, vol. 44, no. August 2007, pp. 1–19, 2008.

[25] A. Tartakovsky and P. Meakin, "Modeling of surface tension and contact angles with smoothed particle hydrodynamics," *Physical Review E*, vol. 72, p. 026301, 2005.

[26] ——, "Pore scale modeling of immiscible and miscible fluid flows using smoothed particle hydrodynamics," *Advances in Water Resources*, vol. 29, no. 10, pp. 1464–1478, 2006.

[27] A. Tartakovsky and A. Panchenko, "Pairwise Force Smoothed Particle Hydrodynamics model for multiphase flow: Surface tension and contact line dynamics," *Journal of Computational Physics*, vol. 305, pp. 1119–1146, 2016.

[28] H. Wendland, "Piecewise polynomial, positive definite and compactly supported radial functions of minimal degree," *Advances in computational Mathematics*, vol. 4, no. 1, pp. 389–396, 1995. [Online]. Available: http://www.springerlink.com/index/L8J8724V5361U767.pdf

[29] W. Dehnen and H. Aly, "Improving convergence in smoothed particle hydrodynamics simulations without pairing instability," *Monthly Notices of the Royal Astronomical Society*, vol. 425, pp. 1068–1082, 2012.

[30] R. A. Gingold and J. J. Monaghan, "Kernel estimates as a basis for general particle methods in hydrodynamics," *Journal of Computational Physics*, vol. 46, no. 3, pp. 429–453, Jun. 1982.

[31] J. P. Morris, P. J. Fox, and Y. Zhu, "Modeling Low Reynolds Number Incompressible Flows Using SPH," *Journal of Computational Physics*, vol. 136, no. 1, pp. 214–226, Sep. 1997.

[32] J. J. Monaghan, "Smoothed particle hydrodynamics," *Reports on Progress in Physics*, vol. 68, no. 8, pp. 1703–1759, Aug. 2005.

[33] K. Batchelor, *An Introduction to Fluid Dynamics*. London: Cambridge University Press, 2000.

[34] L. D. Libersky, A. G. Petschek, T. C. Carney, J. R. Hipp, and F. a. Allahdadi, "High Strain Lagrangian Hydrodynamics," pp. 67–75, 1993.

[35] Y. I. Zhu, P. J. Fox, and J. P. Morris, "A pore-scale numerical model for flow through porous media," *International Journal for Numerical and Analytical Methods in Geomechanics*, vol. 23, pp. 881–904, 1999.

[36] A. Tartakovsky, K. F. Ferris, and P. Meakin, "Lagrangian particle model for multiphase flows," *Computer Physics Communications*, vol. 180, no. 10, pp. 1874–1881, 2009.

[37] D. Holmes, J. Williams, and P. Tilke, "Smooth particle hydrodynamics simulations of low Reynolds number flows through porous media," *International Journal for Numerical and Analytical Methods in Geomechanics*, vol. 35, pp. 419–437, 2011.

[38] P. de Gennes, "Wetting: statics and dynamics," *Reviews of Modern Physics*, vol. 57, no. 3, pp. 827–863, Jul. 1985.